

## RESEARCH ARTICLE

10.1002/2015RS005808

## Key Points:

- HF radar backscatter returns from in front of and behind the radar
- Elevation angles are used to determine backscatter propagation path
- Interpretation of ionospheric phenomena improved by the determination of the direction of origin

## Correspondence to:

A. G. Burrell,  
ab763@le.ac.uk

## Citation:

Burrell, A. G., S. E. Milan, G. W. Perry, T. K. Yeoman, and M. Lester (2015), Automatically determining the origin direction and propagation mode of high-frequency radar backscatter, *Radio Sci.*, 50, doi:10.1002/2015RS005808.

Received 17 SEP 2015

Accepted 13 NOV 2015

Accepted article online 18 NOV 2015

# Automatically determining the origin direction and propagation mode of high-frequency radar backscatter

Angeline G. Burrell<sup>1</sup>, Stephen E. Milan<sup>1</sup>, Gareth W. Perry<sup>2</sup>, Timothy K. Yeoman<sup>1</sup>, and Mark Lester<sup>1</sup>
<sup>1</sup>Department of Physics and Astronomy, University of Leicester, Leicester, UK, <sup>2</sup>Department of Physics and Astronomy, University of Calgary, Calgary, Alberta, Canada

**Abstract** Elevation angles of returned backscatter are calculated at Super Dual Auroral Radar Network radars using interferometric techniques. These elevation angles allow the altitude of the reflection point to be estimated, an essential piece of information for many ionospheric studies. The elevation angle calculation requires knowledge of the azimuthal return angle. This directional angle is usually assumed to lie along a narrow beam from the front of the radar, even though the signals are known to return from both in front of and behind the radar. If the wrong direction of return is assumed, large uncertainties will be introduced through the azimuthal return angle. This paper introduces a means of automatically determining the correct direction of arrival and the propagation mode of backscatter. The application of this method will improve the accuracy of backscatter elevation angle data and aid in the interpretation of both ionospheric and ground backscatter observations.

## 1. Introduction

Coherent scatter high-frequency (HF) radars, such as those that make up the Super Dual Auroral Radar Network (SuperDARN) [Greenwald *et al.*, 1995; Chisham *et al.*, 2007], are sensitive to *E* and *F* region ionospheric irregularities. These radars also detect a significant amount of ground backscatter (groundscatter) via diffuse reflection, which can be used to study the ionosphere below the plasma density peak. Investigations of the ambient and disturbed ionosphere both require accurate knowledge of the radar backscatter locations, which can be obtained with accurate knowledge of the elevation angle of arrival, azimuthal angle off the radar boresite, and the time of flight.

The time of flight for signals to travel from and return to the SuperDARN radars is interpreted as a distance. The HF radar emits a multipulse signal at a frequency between 8 and 20 MHz along a narrow, steerable beam that lies at a specified azimuthal angle from the radar boresite. In standard operations, the returning signals are detected at a gate length of 300  $\mu$ s, translating to distance bins (or range gates) of 45 km. This gate length is a compromise, chosen to provide sufficient frequency and spatial resolution to accurately determine the line-of-sight Doppler velocities.

The vertical angle of arrival, or elevation angle ( $\Delta$ ), can be determined with the aid of an interferometer, a second, smaller antenna array that is displaced from the main radar array. The phase lag ( $\Psi_0$ ) between the signals measured at the two arrays, determined from the cross-correlation function of the combined signals, can be used to calculate the elevation angle [Farley *et al.*, 1981]. The two arrays are typically separated by a distance of 100 m (a distance longer than one wavelength at even the lowest frequency used by SuperDARN), which results in a  $2\pi$  ambiguity in phase lag and aliasing in the elevation angle [Milan *et al.*, 1997; McDonald *et al.*, 2013].

Although the SuperDARN radars are designed to send and receive signals from the forward look direction (the “front lobe” or “front field of view” of the radar), backscatter signals are received from both in front of and behind the radar [Milan *et al.*, 1997; Bland *et al.*, 2014]. Without direction of arrival information, rear field-of-view backscatter is interpreted as originating in the front field of view. Moreover, backscatter assumed to originate from the wrong field of view causes the part of the elevation angle calculation that corrects for the  $2\pi$  ambiguity in phase to fail, causing errors of tens of degrees in the calculated elevation angle.

©2015. The Authors.

This is an open access article under the terms of the Creative Commons Attribution License, which permits use, distribution and reproduction in any medium, provided the original work is properly cited.

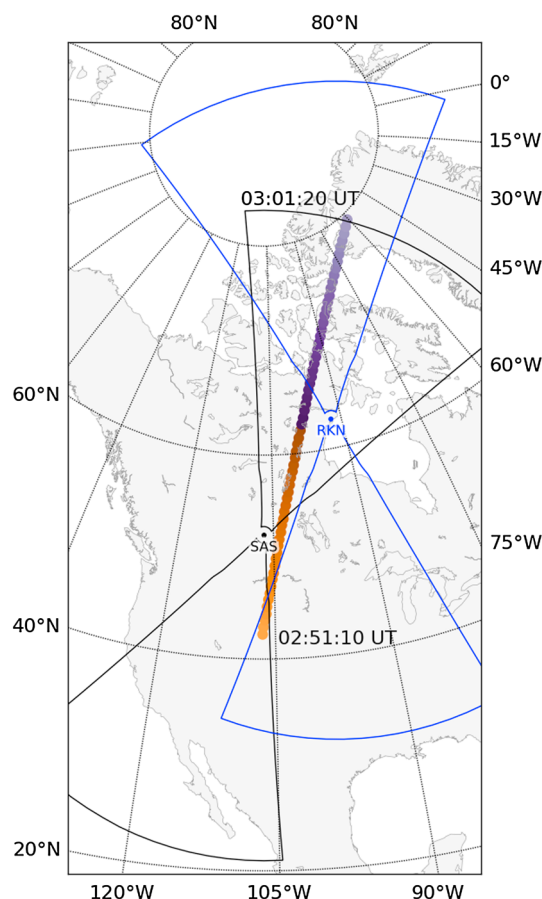


**Figure 1.** CASSIOPE pass (filled circles) over Saskatoon (SAS, black) and Rankin Inlet (RKN, blue) on 5 April 2015 with the area covered by the radar field of views outlined. The earlier times of the satellite pass are in orange, while the later times are in purple. For each SuperDARN radar, the front field of view extends to the north and the rear field of view extends to the south.

Instrument (RRI) [James et al., 2015], a part of the enhance Polar Outflow Probe (e-POP) [Yau and James, 2015] that flies on board the CASCade, Smallsat and IOnospheric Polar Explorer (CASSIOPE) satellite, indicate that the strength of the signal sent behind the radar may be much greater than expected.

RRI measures artificially and naturally generated radio emissions from 10 Hz to 18 MHz. One of its many scientific objectives is to investigate HF radio wave propagation through coordinated experiments with SuperDARN. CASSIOPE often passes in and out of the front and rear fields of view of Canadian SuperDARN radars during its operational periods. The detection of radio emissions at the operational transmission frequencies of the different radars by RRI allows the actual transmission range of the coincident SuperDARN radars to be determined.

One such pass over Saskatoon and Rankin Inlet is shown in Figure 1. In this pass CASSIOPE traveled from the rear fields of view formed by Saskatoon and Rankin Inlet, past each radar, and into the front fields of view. In this map the radar locations, front (northward) fields of view, and rear (southward) fields of view are shown for Saskatoon (SAS) in black and Rankin Inlet (RKN) in blue. The track followed by CASSIOPE is shown by the path of dots, with the time progression indicated by color: orange denotes the starting time of 4 April 2015 02:51:10 UT and purple denotes the ending time of 4 April 2015 03:01:20 UT. The satellite altitude started at 328 km and increased to 443 km. During this period, Saskatoon and Rankin Inlet were operating in modes where they transmitted at  $11.210 \pm 0.001$  MHz and  $11.200 \pm 0.001$  MHz, respectively. RRI observed transmissions at these frequencies from both receiving channels, labeled A and B. The voltage received from these frequency bands are shown in Figure 2 (top and bottom) for channels A and B, respectively. Following the

## 2. Motivation

Standard SuperDARN data analysis assumes that all backscatter returns from the front field of view. This is arguably a reasonable assumption for *F* region ionospheric backscatter, since most radars are directed so that the forward look direction faces regions prone to ionospheric irregularities. However, there is no such expectation for groundscatter, near-range backscatter from meteor ablation, and (to a lesser extent) *E* region ionospheric backscatter.

Another reason that backscatter returning from the rear field-of-view have been largely overlooked is because modeled antenna gain patterns show that the power transmitted to the rear field of view is significantly smaller than the power transmitted to the front field of view. Milan et al. [1997] showed that the power backscatter received from the rear field of view is approximately 20 dB weaker than the backscatter received from the front field of view for log-periodic antennae at transmission frequencies of 10 MHz, and Sterne et al. [2011] showed that the power transmitted to the rear field of view is approximately 33 dB weaker than the backscatter received from the front field of view for twin terminated folded dipole antenna at the same transmission frequency. However, the relative strength of the power transmitted to the front and rear fields of view is known to change with transmission frequency [André et al., 1998; Sterne et al., 2011], becoming more equal as the transmission frequency decreases. In addition, recent observations from the Radio Receiver

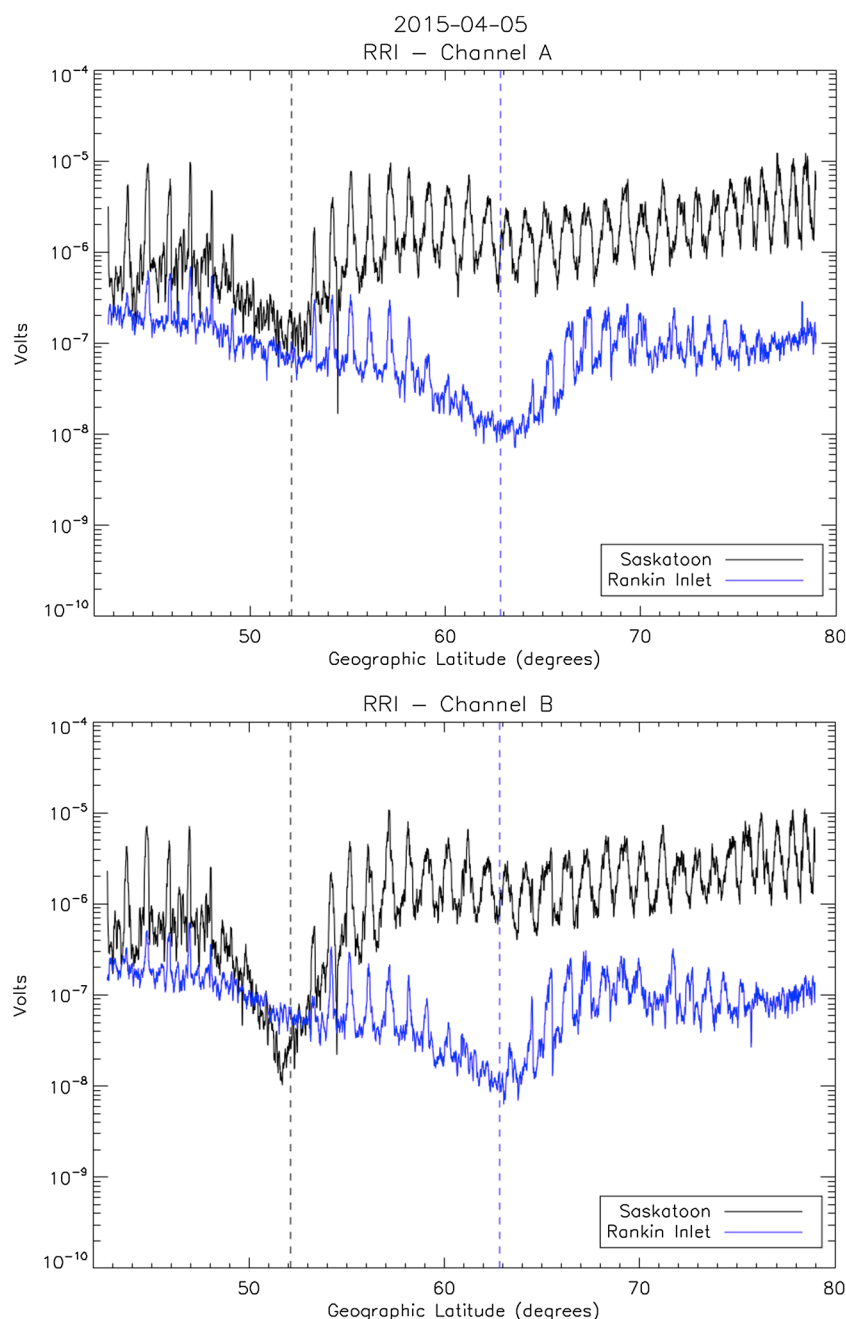


**Figure 2.** Mean voltage measured by RRI over Saskatoon (black) and Rankin Inlet (blue) on 5 April 2015. The SuperDARN radar locations are shown by the dashed vertical lines. (top) Channels A and (bottom) B.

color code in Figure 1, data corresponding to the frequency band used by Saskatoon is shown in black, while the data corresponding to the frequency band used by Rankin Inlet is shown in blue.

The voltages plotted in Figure 2 were processed to obtain a consistent measure of signal strength. They have been scaled to account for variations in distance between the transmitting radar and the receiving channels using the inverse square of the radial distance. After correcting for distance between the transmitter and the receiver, the scaled voltages were smoothed using a 0.16 ms (10 sample) boxcar average. This window is small enough that all major features are visible, including the voltage spikes caused by the SuperDARN radars scanning azimuthally. These peaks occurred approximately once for every degree of latitude CASSIOPE traveled, which is equivalent to a period of about 15 s. In their respective operating modes both radars took approximately 16 s to perform a complete azimuthal scan through the 16 beams comprising their fields of

view. Since the track of CASSIOPE had a very small azimuthal component with respect to either radar, the spacecraft remained within the coverage of a single beam during a scan. The peaks were formed by the power contribution of all 16 beams that participated in a scan. The largest power contribution was from the beam in which CASSIOPE was situated. Even though the beams of SuperDARN radars typically have a half-power width of approximately  $3.24^\circ$ , the RRI instrument is sensitive enough to detect the transmission on any SuperDARN beam, even if CASSIOPE is positioned on the opposite side of the field of view.

Both channels show similar behavior from each radar frequency band. The signal received from Saskatoon peaks behind the radar near  $45^\circ$  latitude, drops off as the satellite flies over the radar, and peaks again at  $57^\circ$  latitude. After the northern peak, the signal drops off over the location of Rankin Inlet, and then increases to a level near the front peak and remains steady. The voltage peaks near the radar show the locations where most signals following  $\frac{1}{2}$ -hop propagation paths were received. The second voltage increase north of the radar marks the point where signals following  $1\frac{1}{2}$ -hop propagation paths were received.

The signal received from Rankin Inlet also shows peaks near the front and rear of the radar. However, a secondary peak at  $45^\circ$  latitude is also observed. This is caused by the satellite orbit, which lies directly in the path of one of the rear field-of-view beams at the start of this section of the orbit and moves just outside the rear field of view as CASSIOPE approaches the radar at Rankin Inlet. There may also be some contribution from Saskatoon, caused by signal leaking across the frequency spectrum, beyond its specified transmission frequency.

The changes in satellite position within the radar fields of view and the presence of signal leakage make it challenging to precisely determine the relative strength of the front and back fields of view for Saskatoon and Rankin Inlet using this pass. However, the presence of strong voltage peaks in front and behind both radars, which have different antennae designs, indicates that backscatter detections in the rear field of view are a clear possibility. This paper outlines an automated method for distinguishing front backscatter from rear backscatter for radars with an interferometer array.

### 3. Method

The origin field of view is determined by examining the consistency of the elevation angle across all beams at a given range gate and along a single beam, using elevation angles calculated for backscatter assumed to originate from both the front and rear fields of view. This is possible because the spatial variations in the elevation angle are different when the field of view is changed. *Milan et al.* [1997] showed that backscatter with the same propagation path and virtual height displays a distinctive pattern when its elevation angle is plotted as a function of beam and range gate, allowing the origin field of view to be determined.

This pattern is easily identified visually, as shown in Figure 3. This figure, a reproduction of Figure 4 in *Milan et al.* [1997], considers each of the 1200 beam and gate combinations in the field of view of a typical SuperDARN radar. Figure 3 (top row) exactly reproduces the figure in *Milan et al.* [1997], which used a flat-Earth approximation in their example, while Figure 3 (bottom row) performs the calculations for a curved Earth. The path length between a ground signal received at the main and interferometer arrays is modeled for each of these beam-gate combinations for  $\frac{1}{2}$ -hop backscatter with a virtual height of 300 km. The phase lag is then aliased to account for the radar sensitivity to phase lags between  $\pm\pi$ . These modeled phase lags are shown for backscatter in Figure 3 (left column).

To calculate the elevation angle, the full path length difference must be reconstructed. This is done by adding integer multiples of  $2\pi$  to the modeled phase lags. Done correctly, the expected elevation angle pattern, which shows the elevation angle decreases with increasing range gate in each region with the same alias, is retrieved (illustrated in Figure 3 (middle column)). If the  $2\pi$  ambiguities are incorrectly handled (such as assuming that backscatter originates from the front field of view when it originates in the rear field of view), then an incorrect pattern in the elevation angle emerges (Figure 3, right column).

Consider the modeled values of the elevation angle in a limited range of distances from the radar (say between range gates 50 and 60). Across all 16 beams, the elevation angles in Figure 3 (middle column) cluster near  $11^\circ$ , while those in Figure 3 (right column) have a broad distribution of values spanning nearly the entire range of possible elevation angles. Also, when the elevation angle is calculated assuming the correct origin field of view, the elevation angle decreases with increasing range gate (apart from jumps caused by aliasing). The detection algorithm presented here uses these characteristics to determine the origin field of view. In essence,

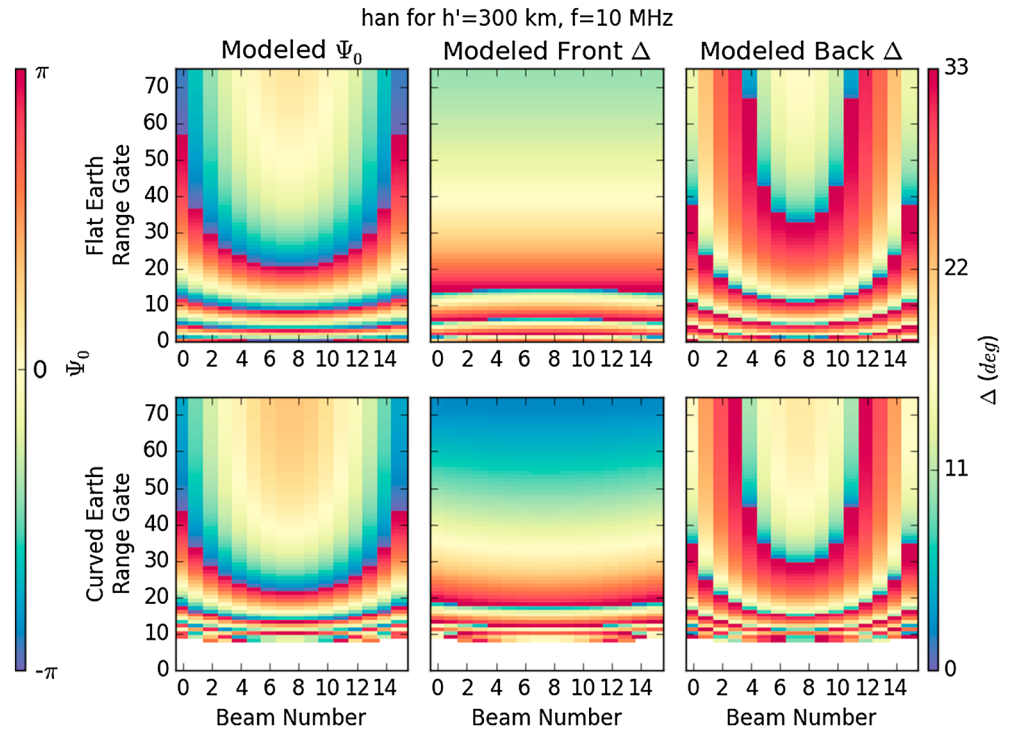


**Figure 3.** (left column) Phase lag, (middle column) elevation angle for backscatter originating from the front field of view, and (right column) elevation angle for backscatter originating from the back field of view for modeled ionospheric backscatter returning from a virtual height of 300 km with a frequency of 10.0 MHz at Hankasalmi. (top row) A flat Earth and reproduces Figure 4 from *Milan et al.* [1997]. (bottom row) A curved, spherical Earth.

it tests the assumption that backscatter originates from each field of view and assigns the direction that is most consistent with the modeled values.

The detection algorithm presented here uses six steps to determine the origin field of view for ground and ionospheric backscatter. The first four steps examine the variations in elevation angle and virtual height, assigning points to either the front or rear field of view. This is done by calculating the virtual height, examining the variations in elevation angle across all beams for backscatter at each range gate, testing the realism of the virtual heights for unassigned backscatter in each field of view, and, finally, examining the variations in elevation angle along a single beam for any remaining backscatter without an assigned field of view. The final two steps take advantage of the tendency of ground and ionospheric backscatter to form spatially coherent structures that slowly evolve over time by removing any field of view assignments that are not consistent with the surrounding backscatter detections.

The following subsections discuss these steps in detail. The results of each step in the field-of-view identification process are illustrated using data from Hankasalmi on 16 September 1996, between 05:00 and 06:00 UT. This time and location were shown as an example because it is a period with several different backscatter propagation modes. It also contains regions with backscatter returning from coherent structures in each field of view.

### 3.1. Step 1: Calculate Virtual Height

The first step in the automated field-of-view detection calculates the virtual height ( $h'$ ) for each backscatter observation in both fields of view using equation (1). This equation accounts for the curvature of the Earth but assumes that the Earth is a sphere rather than an oblate spheroid. The terrestrial radius ( $R_{\oplus}$ ) is set as the terrestrial radius at the radar location.

$$h' = \sqrt{d^2 + R_{\oplus}^2 + 2dR_{\oplus} \sin \Delta} - R_{\oplus} \quad (1)$$

In the above equation,  $d$  is the distance along the signal path to the first ionospheric refraction or reflection point for ionospheric and ground backscatter data, respectively. This distance assumes a straight-line propagation path between the radar and the ionospheric reflection point, and the ionospheric refraction point



**Table 1.** Ionospheric Layer Altitude Limits and Allowed Propagation Paths

Layer	Virtual Height (km)		Hops
	Minimum	Maximum	
D	75	115	$\frac{1}{2}$
E	115	150	$\frac{1}{2}$ , 1, $1\frac{1}{2}$
F	150	900	All

and the ground. For  $\frac{1}{2}$ -hop ionospheric backscatter, this distance is the range gate expressed in kilometers. However, for propagation paths where the transmitted signal is reflected off the ground (such as groundscatter or  $1\frac{1}{2}$ -hop ionospheric backscatter),  $d$  may be found by dividing the range gate, expressed in kilometers, by double the hop number. For example,  $d$  for 1-hop groundscatter is half the distance given by the range gate.

Significant errors in the virtual height calculation are introduced by errors in the elevation angle, error in  $d$ , by the assumption that the propagation follows straight-line paths, and (for propagation paths larger than one hop) by the assumption that the reflection and refraction height along the propagation path is the same. Even with these sources of error, the virtual height can be used to successfully separate backscatter into groups by propagation path and virtual height, since for a given period of time backscatter returning from the same geographic area is likely to return along similar propagation paths and so have similar characteristics whether or not they are objectively true. This assumption begins to break down as the number of hops increases. This study considers propagation paths up to three hops, encompassing the vast majority of backscatter observed by SuperDARN.

The determination of the origin field of view begins by computing the virtual height twice, using elevation angles calculated for backscatter originating in both the front and rear fields of view. In each field of view this virtual height is examined to ensure that the appropriate distance was used. Initially, backscatter is assumed

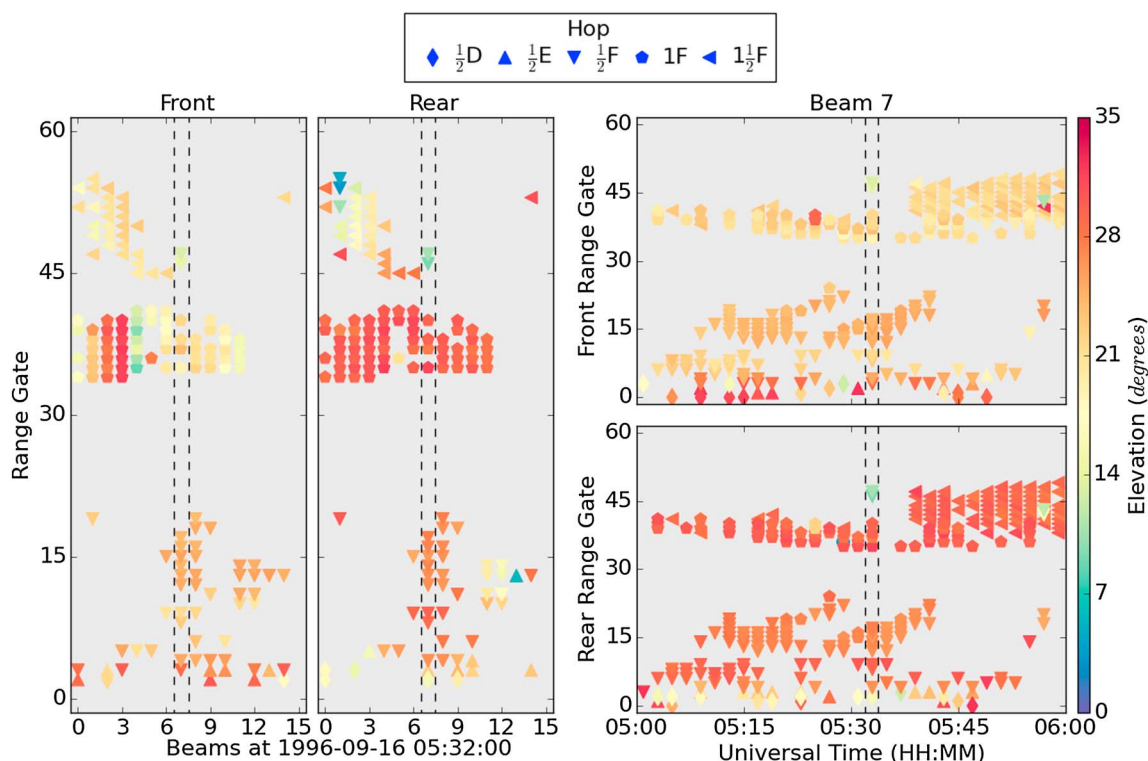


**Figure 4.** Elevation angle calculated for backscatter originating from the front and rear field of view at Hankasalmi for a scan at 05:32 UT and beam 7 from 05:00-06:00 UT on 16 September 1996. The ionospheric region and hop for each backscatter point is indicated by the shape of the marker.

to have a  $\frac{1}{2}$ -hop or 1-hop propagation path, depending on whether it is ionospheric backscatter or groundscatter. However, if the resulting virtual height is higher than the allowed upper limit (set at 900 km to allow for differences between the actual and virtual altitude, which can become very large when the signal travels horizontally for long distances along Pedersen rays [Chisham *et al.*, 2008]), then the propagation path is increased by one hop and the virtual height is recalculated. If this does not succeed in producing a realistic virtual height, then the entire process is attempted one last time, but using an elevation angle calculated with an alias of  $2\pi$  (the most commonly encountered alias).

After these virtual height adjustments are made, the backscatter are further separated into ionospheric regions. Following the work of Chisham *et al.* [2008] and Chisham and Freeman [2013], backscatter is attributed to the *D*, *E*, or *F* region if it has a virtual height that falls within the altitude limits outlined in column 2 of Table 1 and a propagation path that falls within the hop limits outlined in column 3 of the same table. Backscatter that cannot be attributed to one of these ionospheric layers is removed from consideration for that field of view.

Figure 4 shows the elevation angle calculated from the front and rear field of view for Hanksalmi on 16 September 1996. The two plots in Figure 4 (left) show the front and rear fields of view for a scan taken at 05:32 UT, while the two plots in Figure 4 (right) show the front and rear fields of view for beam 7 as a function of time for the interval of 05:00–06:00 UT. The shape of each backscatter point indicates the propagation path assigned using the process described in the previous paragraph.

Comparing elevation angle patterns of the scans in Figure 4 to the modeled front and rear fields of views in Figure 3, the elevation angle variations at each range gate across all beams indicate that the  $1F$ -hop groundscatter originates from the rear field of view, while the  $1\frac{1}{2}F$ -hop ionospheric backscatter at the furthest range gates originates from the front field of view. This may seem counterintuitive, since one typically expects to see both  $1F$  and  $1\frac{1}{2}F$  backscatter returning from the same field of view. After all, if a  $1\frac{1}{2}F$  propagation path exists, the  $1F$  propagation path must exist as well. However, it is not improbable that the groundscatter returning to the radar would have a stronger signal from the rear field of view than the front field of view. Several physical conditions make this possible, including a more specular reflection point or a denser ionosphere to the rear of the radar.

The  $\frac{1}{2}D$  and  $\frac{1}{2}E$  ionospheric backscatter appears to be mixed between the two fields of view, with inconsistent elevation angles at any given range gate across all beams. The  $\frac{1}{2}F$  backscatter between range gates 10–20, on the other hand, has consistent elevation angles across all beams in the front field of view, and a wide range of elevation angles in the rear field of view. When examining the elevation angle variations for a single beam over time, there is less variation in elevation angle. There are some points, however, (such as the  $\frac{1}{2}F$ -hop backscatter at 05:32 near range gate 45) which do not match the surrounding backscatter in space or time.

### 3.2. Step 2: Examine Elevation Angle Variations at Each Range Gate

The second step in this detection algorithm is to examine the variations in the elevation angle for a scan of backscatter across all beams at each range gate. Backscatter are grouped by range gate, propagation path, and virtual height. A sliding window of between 2 and 20 gates (a larger window is used as distance from the radar increases and the accuracy of the range gate decreases [Yeoman *et al.*, 2001]; exact window widths are specified in columns 1 and 2 of Table 2) is used to gather backscatter from all beams for the specified hop. In order to evaluate azimuthal variations (the variations across all beams), the virtual height must be restricted as well. Instead of using windows at fixed virtual heights, backscatter are grouped together by examining the distribution of virtual heights in each field of view.

The process used to establish virtual height windows is illustrated in Figure 5. Figure 5 (top row) shows the virtual heights for  $\frac{1}{2}F$ -hop backscatter gathered at range gate 30 for the front and rear fields of view, with the front field of view in Figure 5 (top left) and the rear field of view in Figure 5 (top right). Figure 5 (bottom left and bottom right) shows histograms of the virtual heights for the front and rear fields of view. The histograms are used to establish virtual height windows centered at the heights, where backscatter are most likely to occur. A Gaussian curve is fit to each peak in the histogram, and the upper and lower limits of the virtual height window are set to fall within three standard deviations of the fitted maxima. Additional windows are added to encompass any points that fall outside of these established limits. When multiple peaks are detected, their upper and lower limits may overlap. In instances where the overlap is large enough to encompass the peak of another distribution, the upper and lower limits of the smaller peak are adjusted to remove this overlap. If no peaks can be identified, but a global maximum with at least three points exists (as may be the case if a peak

**Table 2.** Field-of-View Scan Windows

Applied Range Gates	Window Widths	
	Initial	Extended
1–5	2	5
5–25	5	8
25–40	10	13
40–76	20	23

spans multiple height bins), this global maximum is used to fit a Gaussian curve. Otherwise, virtual height windows are set to span the entire range of heights in windows with widths of 50 km (if the central range gate is less than 45) or 150 km (if the central range gate is 45 or greater).

Once the appropriate backscatter have been gathered, the behavior of the elevation angle is examined in each field of view. Because the algorithm is looking for a consistent elevation angle across all beams, this examination is only performed if there is backscatter from at least three beams in the range gate, propagation path, and virtual height window. If there are data from enough beams, a linear regression is performed on the elevation angles. When a linear regression is performed on elevation angles calculated using the appropriate field of view, the slope will be negative and the standard deviation of the difference between the linear fit and the elevation angles will be small. Thus, backscatter is assigned to a field of view when three conditions are met. First, the slope of the linear regression must be flat or negative. Second, the standard deviation of the difference between the linear fit and the elevation angles are required to be less than or equal to  $3^\circ$ . Third, the backscatter being evaluated lies within three standard deviations of the linear fit (the z score of the backscatter is  $\pm 3$ ). If these criteria are met for both fields of view, the field of view with the smaller standard deviation and a better z score is chosen.

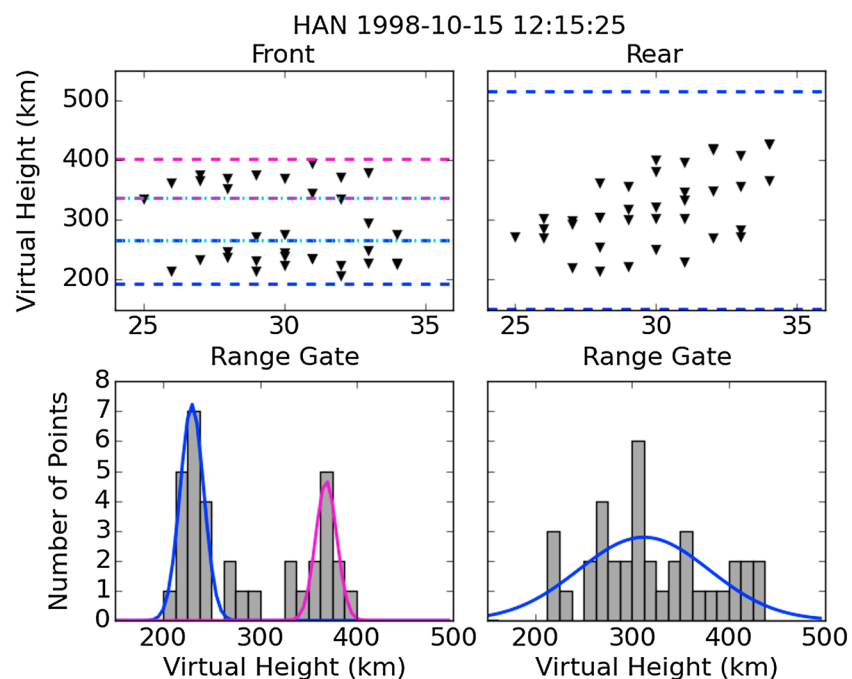


**Figure 5.** Virtual height distribution for  $\frac{1}{2}$  F-hop backscatter centered at range gate 30 at Hankasalmi for a scan at 12:15 UT on 15 October 1998. (top row) The virtual heights at each range gate and (bottom row) the distribution of backscatter at these heights. (left column) The front field of view is shown, and (right column) the rear field of view is shown. Overlaying the histograms are the Gaussian fits used to determine the virtual height windows. The resulting virtual height windows are plotted as dashed lines with the same colors in Figure 5 (top row). In Figure 5 (top left), an additional region, denoted by dotted cyan lines, spans the gap between the two regions assigned by the Gaussian fits.



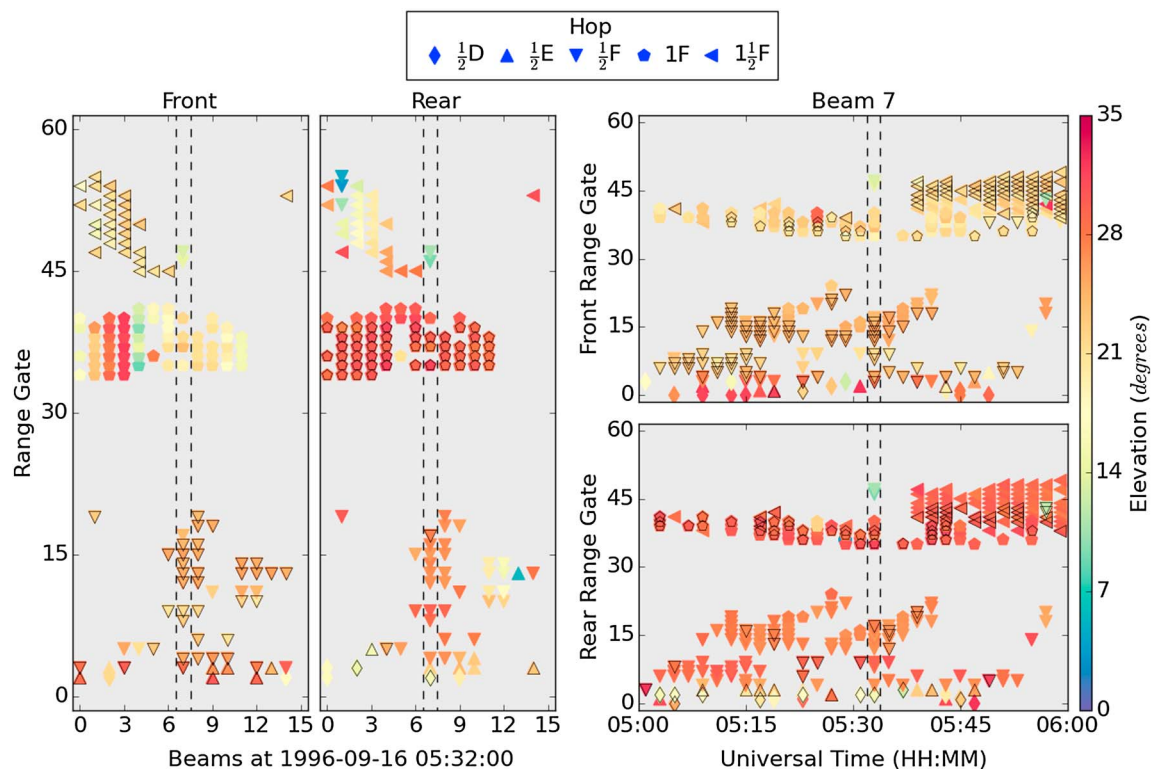


**Figure 6.** Elevation angle calculated for backscatter originating from the front and rear field of view at Hankasalmi for a scan at 05:32 UT and beam 7 from 05:00 to 06:00 UT on 16 September 1996. The ionospheric region and hop for each backscatter point is indicated by the shape of the marker. Black outlines show points that have been identified as originating in the selected field of view by evaluating the elevation angles for range gate, virtual height, and propagation path windows in each scan.

Figure 6 builds from Figure 4, adding a black outline to backscatter assigned to each field of view by this step in the detection algorithm. Note that the  $1F$  groundscatter and  $1\frac{1}{2}F$ -hop ionospheric backscatter, which clearly exhibit patterns identifying the origin field of view, were both assigned to the correct field of view. The near-range  $\frac{1}{2}$ -hop backscatter has been identified as originating mostly from the front field of view, though much of the backscatter has not been assigned an origin field of view at all. Examining the fields of view for beam 7 at different times shows that this scan is typical of those seen at other times. The  $1\frac{1}{2}F$  backscatter is assigned primarily to the front field of view, the  $1F$  groundscatter is assigned primarily to the rear field of view, and the  $\frac{1}{2}$ -hop backscatter has the largest quantity of unassigned points, especially at the nearest range gates.

### 3.3. Step 3: Test the Virtual Height of Unassigned Backscatter

Since not all backscatter observations will be assigned to a field of view using the above method, additional measures must be taken, especially at the nearest range gates. At these range gates, the virtual height alone can sometimes be used to determine the origin field of view. This test takes advantage of the physical limits of the bottomside ionosphere.

Virtual heights calculated for both fields of view close to the radar often differ by 100 km or more, causing a virtual height in one field of view that falls well short of the bottom of the  $D$  region. Backscatter with a physically realistic virtual height in only one field of view is thus assigned to that field of view for range gates within 500 km of the radar. At these distances, aliasing is not typically a problem.

Figure 7 builds from Figure 6, showing the backscatter assigned each field of view after applying Step 3 outlined in black and the backscatter assigned by Steps 1 and 2 as black dots. Comparing points with black outlines and dots shows that this step has identified all the backscatter that had valid virtual heights (and elevation angles) in only one field of view. For example, previously unassigned  $\frac{1}{2}D$ -hop backscatter at beams 2 and 14, range gate 1 are now identified as returning from the front field of view.

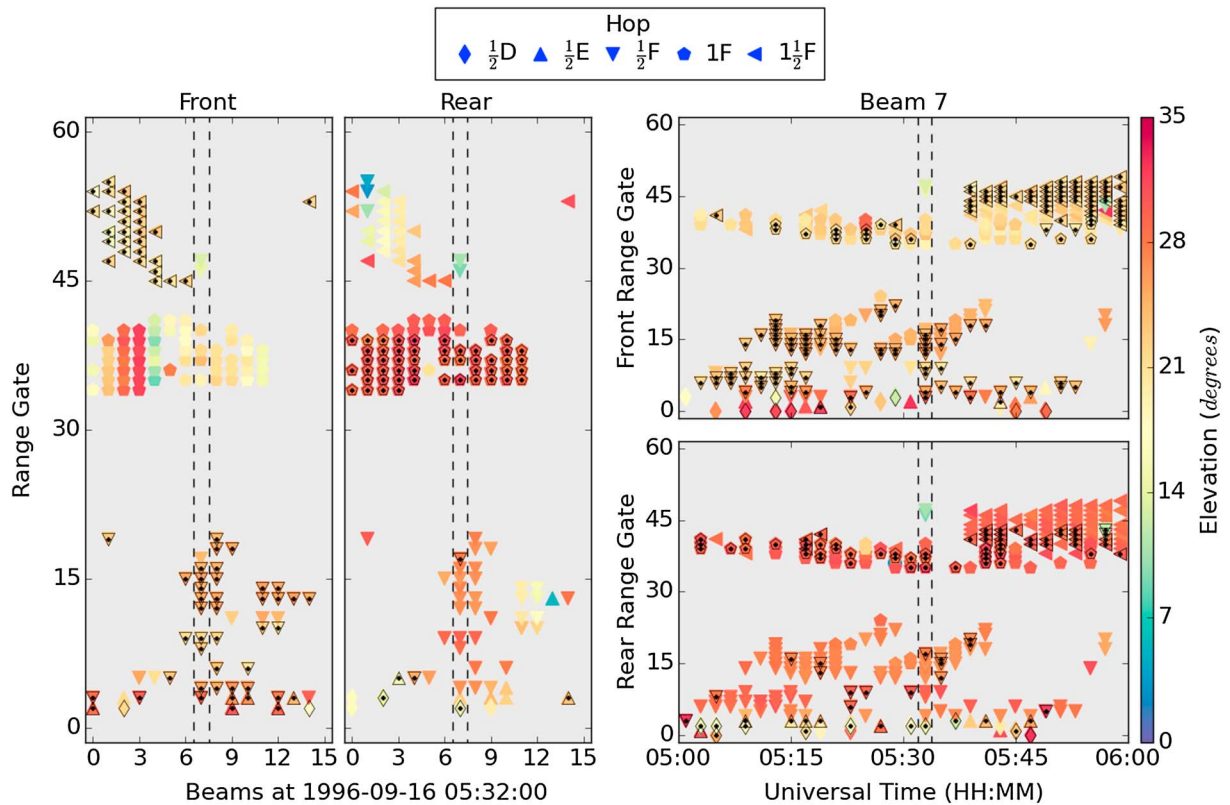


**Figure 7.** Elevation angle calculated for backscatter originating from the front and rear field of view at Hankasalmi for a scan at 05:32 UT and beam 7 from 05:00 to 06:00 UT on 16 September 1996. The ionospheric region and hop for each backscatter point is indicated by the shape of the marker. Black dots show points that have been identified as originating in the selected field of view by evaluating the elevation angles for range gate, virtual height, and propagation path windows in each scan. Black outlines include these points as well as backscatter points that only have a realistic virtual height in one field of view.

### 3.4. Step 4: Examine Elevation Angle Variations Along Each Beam for Unassigned Backscatter

The last step in assigning an origin field of view is to consider the elevation variations along each beam. The elevation angle variations are tested using the same procedure described in Step 2. The only difference is in the backscatter selection criteria. For each unassigned backscatter point, elevation angles are gathered from extended range gate windows, specified by columns 1 and 3 in Table 2. As before, backscatter must come from the same propagation path. At this step, limits in the virtual height are not considered. Instead only backscatter from a single beam is used. Although this test is only performed if there is backscatter without an assigned field of view, all the gathered backscatter are reevaluated using the standard deviation of the backscatter about the linear regression and the individual z scores when the slope of the linear regression is negative.

Figure 8 builds from Figure 7, showing the backscatter assigned each field of view after applying Step 4 outlined in black and the backscatter assigned by Steps 1–3 as black dots. Comparing points with black outlines and dots in the scans in Figure 7 (left) shows that this step has assigned fields of view for almost all the remaining unassigned backscatter. Some of these assignments are expected, such as the 1F groundscatter at beams 2–4, range gate 39 to the rear field of view. Other assignments, though, such as the  $\frac{1}{2}F$  backscatter at beams 11 and 12, range gate 11 are clearly appropriately assigned if only the elevation angle along the beam are considered but not if the azimuthal variations along all beams are taken into account.

### 3.5. Steps 5 and 6: Test for Consistency

Once a field of view has been assigned to as many backscatter points as possible, the spatial and temporal consistency of these assignments can be tested. Both ionospheric and ground backscatter tend to form spatially coherent structures that slowly evolve over time. Thus, the assigned fields of view can be tested to ensure that these coherent structures are not split between the two fields of view.

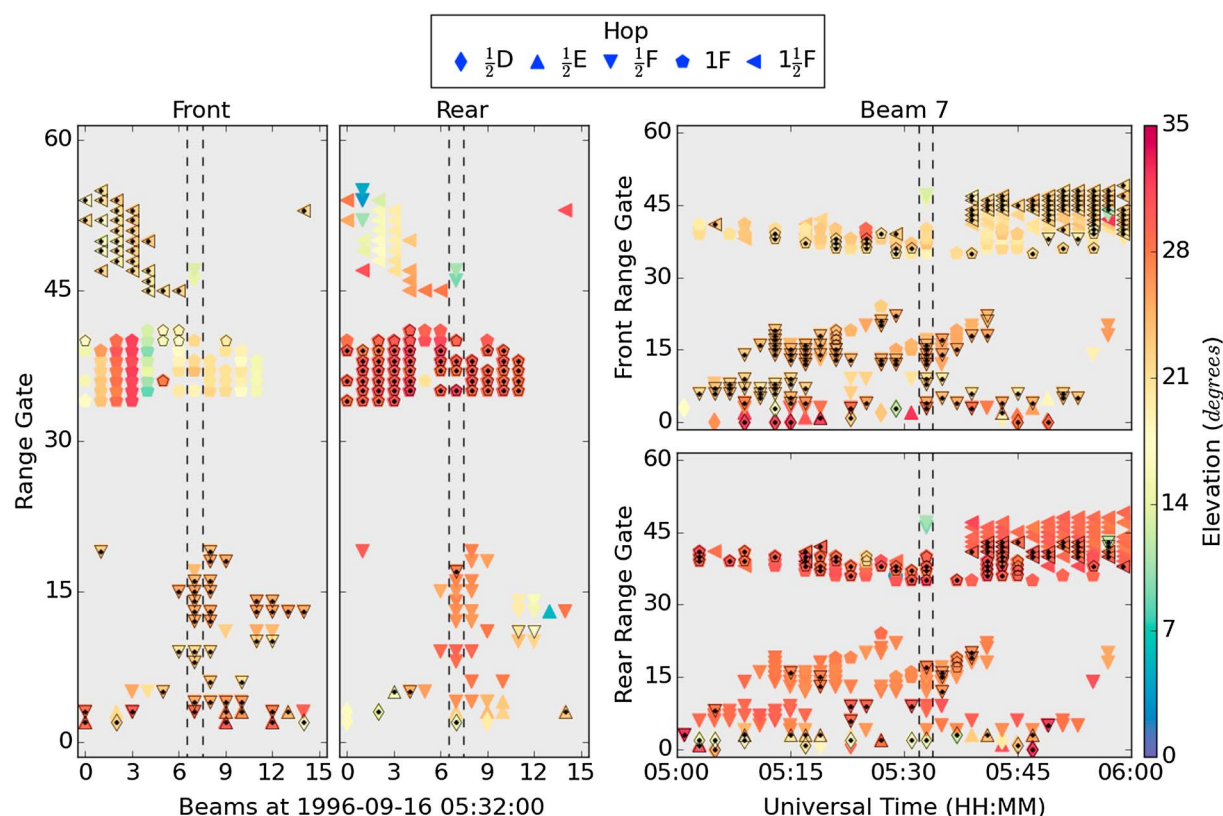


**Figure 8.** (left) Elevation angle calculated for backscatter originating from the front and rear field of view at Hankasalmi for a scan at 05:32 UT and (right) beam 7 from 05:00 to 06:00 UT on 16 September 1996. The ionospheric region and hop for each backscatter point is indicated by the shape of the marker. Black dots show points that have been identified as originating in the selected field of view by evaluating the elevation angles for range gate, virtual height, and propagation path windows in each scan, as well as those that only have a realistic virtual height in one field of view. Black outlines include these points as well as backscatter points whose elevation angles were evaluated along a single beam.

This test is performed at each range gate and beam for backscatter points with the same propagation path within the extended range gate window specified in columns 1 and 3 in Table 2. When examining spatial structures, backscatter is gathered for three beams at a time. When examining temporal structures, backscatter is gathered for a single beam in a 20 min window. The spatial continuity is tested at all times before the temporal continuity is tested.

In each propagation path, range gate, beam, and time window the number of points in each field of view is calculated, allowing each backscatter point to be flagged as being part of a structure, being an outlier, or being part of a mixed field of view region. Backscatter is flagged as being part of a structure if over two thirds of the points are found to lie in one field of view, and the point being considered originates from that field of view. This fraction of points was chosen to strike a balance between allowing regions of mixed propagation paths and reducing incorrect field of view assignments. If a structure is identified and the point being considered originates from the opposite field of view, it is flagged as an outlier. If less than two thirds of the backscatter originate from the same field of view, all the points are flagged as lying in a mixed region.

After performing this test on all backscatter points for a scan (when testing the spatial continuity) or beam (when testing the temporal continuity), the number of times each point is found to be an outlier is examined, unless the backscatter lies within 500 km of the radar and only has a valid virtual height in one field of view. Points that were tagged as outliers at least once are examined further. If they were also tagged as belonging to a cluster of backscatter in the same field of view less times than they were tagged as being either an outlier or part of a mixed field of view, their field of view assignment is changed. If the outlying backscatter point had previously met the criteria for the opposite field of view as outlined in Step 3 and the number of times it was identified as an outlier is greater than both the number of times it was seen in an area of mixed backscatter and the number of times it was an inlier, then the outlying backscatter can be reassigned to the field of view shared by the surrounding backscatter points. However, the assigned field of view may only be changed once. If the

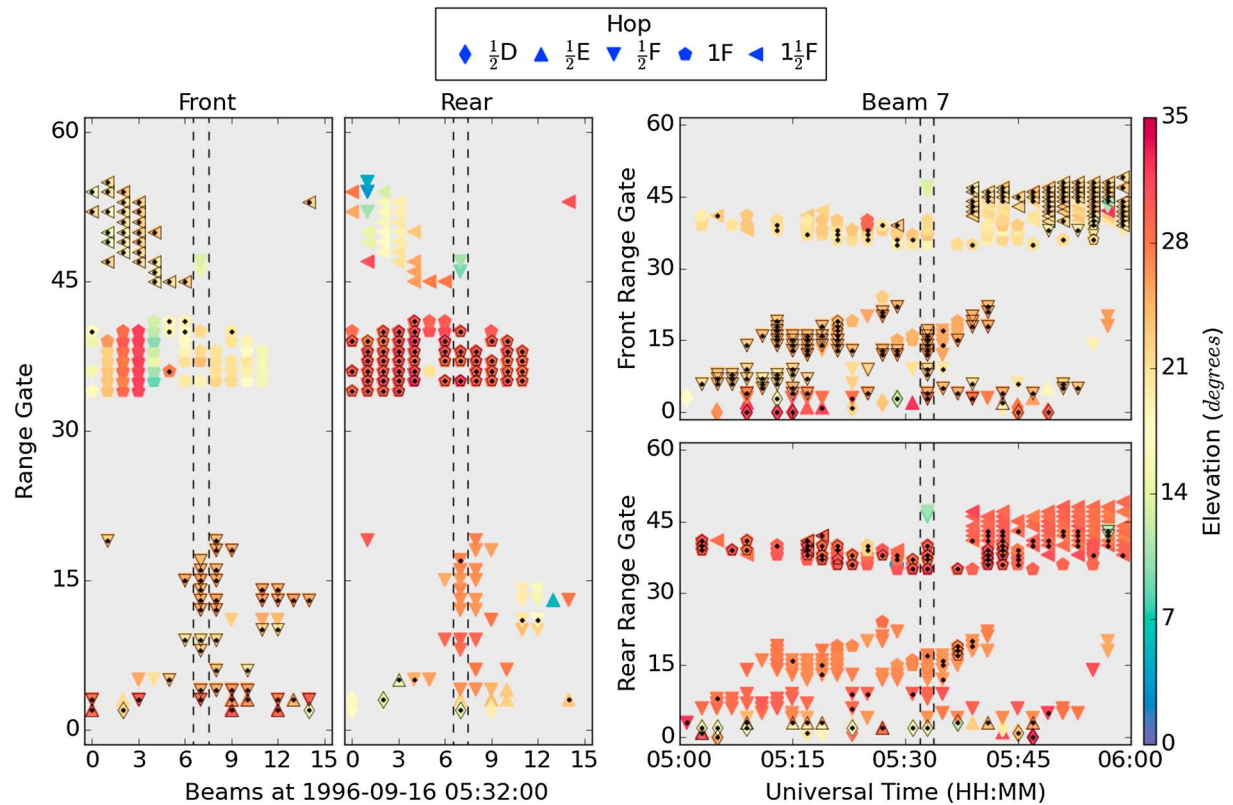


**Figure 9.** Elevation angle calculated for backscatter originating from the front and rear field of view at Hankasalmi for a scan at 05:32 UT and beam 7 from 05:00 to 06:00 UT on 16 September 1996. The ionospheric region and hop for each backscatter point is indicated by the shape of the marker. Black dots show points that have been identified as originating in the selected field of view by evaluating the elevation angles for range gate, virtual height, and propagation path windows in each scan, as well as those that only have a realistic virtual height in one field of view. Black outlines show the final field of view assignments.

scan continuity test changes the origin field of view designation and this new designation fails the temporal continuity test, the backscatter is not assigned to either field of view.

Figure 9 builds from Figure 8, showing the final backscatter assignments for each field of view in black outlines and the backscatter assigned by completing Steps 1–4 as black dots. Focusing on the points discussed in the previous subsection, Figure 9 shows that  $\frac{1}{2}F$ -hop backscatter at beams 11 and 12, range gate 11 have been removed from both fields of view. The  $1F$  groundscatter assigned to the rear field of view remains assigned to that field of view, and the few points assigned to the front field of view have been removed. Indeed, the small portions of  $1F$  groundscatter assigned to the front field of view between range gates 30 and 45 have all been removed or reassigned to the rear field of view from the beginning of this groundscatter formation near 05:00 UT up to the point that it disappears near 05:45 UT. Likewise, the  $1\frac{1}{2}F$  backscatter assigned to the rear field of view after 05:30 have been removed or reassigned to the front field of view.

#### 4. Validation

Figure 9 shows that the field of view detection algorithm does a good job consistently identifying coherent structures in each field of view and can also handle backscatter originating with equal probability in both the front and rear field of view. However, not all backscatter is successfully assigned to an origin field of view. It is also conceivable that some of the field of view assignments are wrong. In this section the field of view detection algorithm is tested by using observations of backscatter with a known location.

The front field of view of the SuperDARN radars at Hankasalmi and Pykkvibær both cover the ionosphere above Tromsø (Figure 10), where the European Incoherent SCATter (EISCAT) ionospheric heater is located. Yeoman *et al.* [2001] used observations from Hankasalmi and Pykkvibær of an ionospheric heating event on 15 October 1998 to evaluate the accuracy of the SuperDARN time-of-flight measurements and investigate



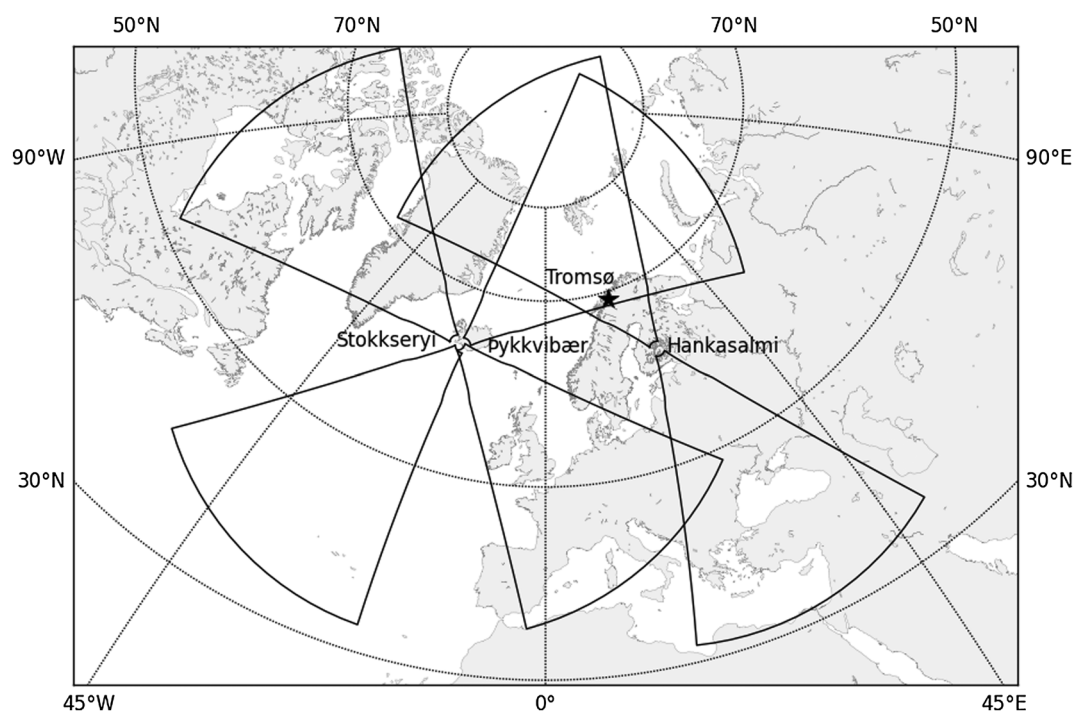


**Figure 10.** Front and rear fields of view for the three European SuperDARN radars: Hankasalmi, Pykkvibær, and Stokkseryi. The location of the ionospheric heater at Tromsø is marked by a black star.

possible propagation paths. Applying the field-of-view detection algorithm to this data set shows  $\frac{1}{2}F$ -hop detections from beam 5 at Hankasalmi and  $1\frac{1}{2}F$ -hop detections from beam 15 at Pykkvibær. Figure 11 plots the power and elevation angles for beam 5 at Hankasalmi (left column) and beam 15 at Pykkvibær (right column). Figure 11 (first row) reproduces the first and third panels of Plate 1 in Yeoman *et al.* [2001]. Figure 11 (second and third rows) shows the front and rear field of views, respectively, with the elevation angles for points assigned to each field of view. Figure 11 (fourth row) shows the backscatter not assigned to either field of view, with propagation paths and elevation angles calculated assuming the backscatter originated from the front field of view. Note that all backscatter at Hankasalmi is manually flagged as ionospheric backscatter, since the heater-induced irregularities typically have very low line-of-sight velocities when observed from Hankasalmi and so are easily confused with groundscatter. The narrow azimuthal spread of the heater-induced ionospheric backscatter, which at most spanned three beams, provided an additional challenge to the field of view determination algorithm.

Examining Figure 11 (second and third rows) shows that the vast majority of backscatter is correctly assigned to the front field of view. No backscatter is incorrectly assigned to the rear field of view at range gates associated with heater backscatter at Hankasalmi, while a handful of ionospheric backscatter points are incorrectly assigned to the rear field of view at range gates associated with heater backscatter at Pykkvibær. To examine these assignments quantitatively, the number of ionospheric backscatter points are gathered between range gate 25–35 at Hankasalmi, as well as range gates 34–39 and 50–59 at Pykkvibær. These range gates encompass the area of  $\frac{1}{2}F$ -hop heater backscatter observed from Hankasalmi, the area of  $1\frac{1}{2}F$ -hop heater backscatter observed from Pykkvibær, and the two areas where  $2\frac{1}{2}F$ -hop heater backscatter were observed from Pykkvibær. The percentage of points correctly assigned to the front field of view, incorrectly assigned to the rear field of view, and not assigned to either field of view for the beams shown in Figure 11, as well as all beams that detect backscatter from the heater-induced irregularities, are shown in Table 3.

The algorithm to determine the appropriate field of view performs well in both cases, though the results are better at Hankasalmi. This can be attributed, in part, to the mix of propagation paths detected by Pykkvibær. At Pykkvibær, the range gates where heater backscatter are detected are mixed with groundscatter and show large variations in signal power. The ionospheric backscatter returning from the front field of view is identified

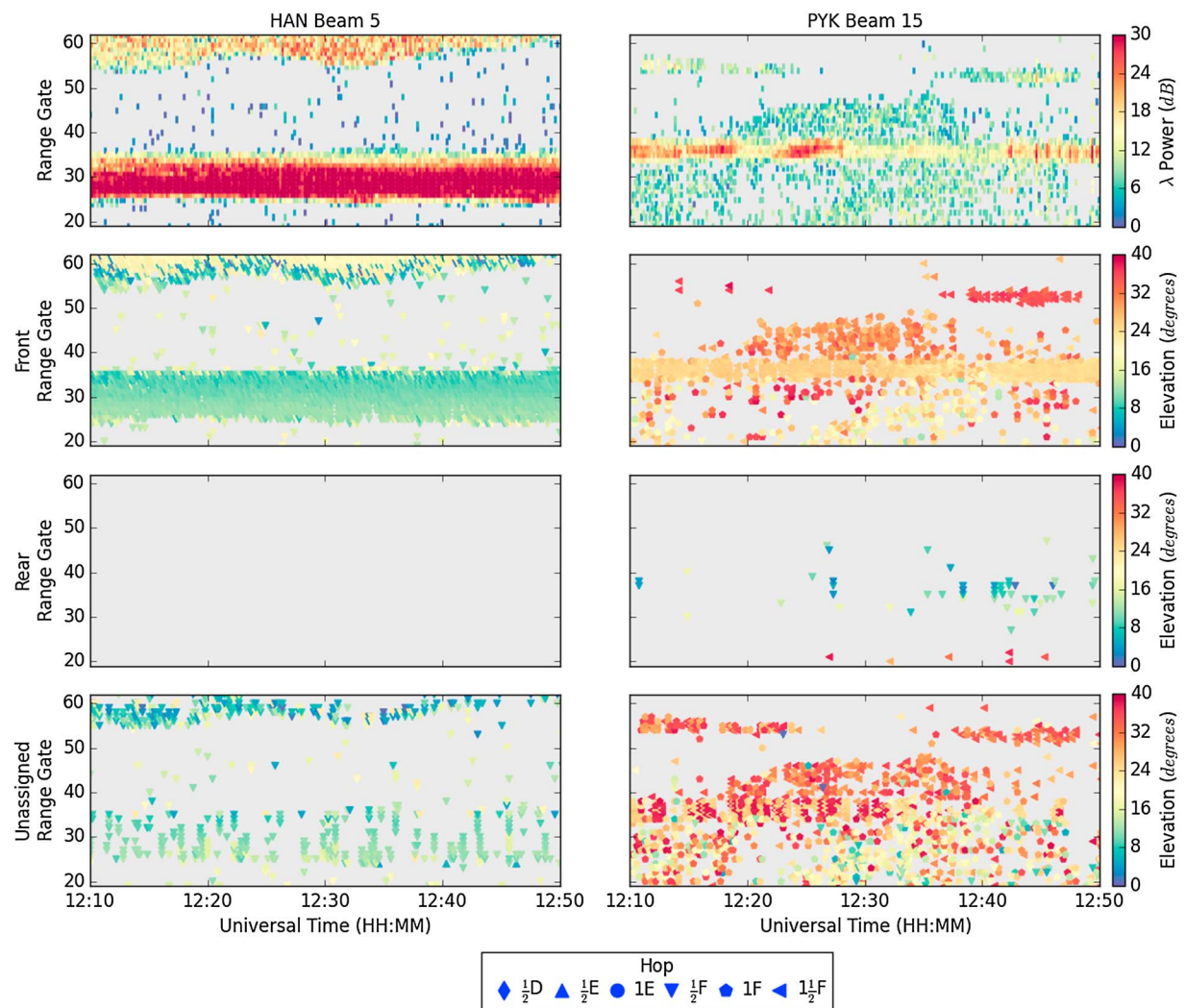


**Figure 11.** Power and elevation angle for (left column) beam 5 at Hankasalmi (HAN) and (right column) beam 15 at Pykkvibær (PYK). (first row) The backscatter power and (second and third rows) the elevation angles for the front and rear fields of view. (fourth row) The elevation for the front field of view for backscatter not assigned to either field of view. The shape of each point corresponds to the backscatter propagation path.

as entirely  $1\frac{1}{2}F$ -hop between range gates 34–39 and 50–59, while the ionospheric backscatter incorrectly assigned to the rear field of view, or not assigned to either field of view, is labeled as a mix of  $\frac{1}{2}F$ - and  $1\frac{1}{2}F$ -hop. The lack of  $2\frac{1}{2}F$  propagation paths between range gates 34–39 and 50–59 (and the presence of  $1\frac{1}{2}$  propagation paths at range gates greater than 50) disagrees with the more rigorous propagation path analysis performed by Yeoman *et al.* [2001]. This reveals a weakness in the propagation path determination. As the upper limit of the  $F$  region virtual height is set to accommodate Pedersen propagation paths, two and one-half hop and greater propagation paths in the  $E$  and  $F$  region are extremely unlikely to be attributed. Instead of

**Table 3.** Field-of-View Assignments for Ionospheric Backscatter Returning From Heater-Induced Irregularities

Radar Beam	HAN		PYK		Both All
	5	4–6	15	13–15	
Total Points	2107	5660	941	2082	7742
Front	86.43%	84.33%	64.93%	60.14%	77.82%
Rear	0.00%	0.00%	3.08%	7.78%	2.09%
Unassigned	13.57%	15.67%	31.99%	32.08%	20.09%



$2\frac{1}{2}F$ -hop backscatter, a  $1\frac{1}{2}F$ -hop propagation path with a long period of horizontal travel after the first hop is preferred. In addition, multiple-hop propagation paths that have different peak heights (such as  $1\frac{1}{2}FE$ -hop backscatter) are not allowed. This limitation is not as problematic as it may appear, the longer and mixed region propagation paths make up a small portion of the total SuperDARN backscatter [Chisham *et al.*, 2008].

Another difference between the performance at Hankasalmi and Pykkvibær is the greater amount of low-power backscatter (defined as backscatter with power at or below 10 dB) at range gates associated with heater-induced backscatter. This did not appear to play a role in identifying the wrong field of view: 27.16% of the data incorrectly assigned to the rear field of view had low signal power, while 22.92% of the data correctly assigned to the front field of view had low signal power. However, close to half (40.11%) of the ionospheric backscatter not assigned a field of view had signal powers at or below 10 dB. Other factors influencing the poorer performance of the field of view determination algorithm at Pykkvibær when compared to Hankasalmi is the position of the heater backscatter near the edge of the radar field of view. Recall that the heater-induced ionospheric backscatter spanned at most three beams, less than are typically seen with naturally occurring ionospheric backscatter, and narrower structures are more difficult to test for spatial trends and consistency (Steps 1–5) than wider structures.

## 5. Performance

The performance of the field-of-view detection algorithm can be judged in a more qualitative method under a variety of ionospheric conditions. This section presents three examples with different types of backscatter whose origin field of view can be determined by physical reasoning. The first example shows a period of time when the auroral oval expands, causing ionospheric backscatter to pass over the radar. Next, the groundscatter at Hankasalmi, which shows a distinct double-sunrise signature, is presented. Finally, the assignment of meteor ablation is shown to produce a more spatially consistent velocity pattern when the origin field of view is known.

### 5.1. Geomagnetic Storm

This example shows previously unpublished SuperDARN data for a period during a geomagnetic storm, in which the  $Dst$  ranged from  $-14$  to  $-65$  nT. During this period, it appears that the auroral oval has expanded to latitudes south of Pykkvibær. Figure 12 shows the Doppler line-of-sight velocities measured from beam 0 at Pykkvibær on 10 October 1997. Figure 12 (first panel) shows the velocity from all backscatter points, regardless of field of view, while Figure 12 (second to fourth panels) shows the backscatter for the front, rear, and unassigned fields of view in descending order, with propagation path indicated by marker shape. In all cases, the velocity shown is the Doppler line-of-sight velocity for the front field of view. This means that positive (blue) velocities indicate a southwest drift for backscatter in front of the radar and a northeast drift for backscatter behind the radar. Conversely, the negative (red) velocities indicate a northeast drift for backscatter in front of the radar and a southwest drift for backscatter behind the radar. The black vertical lines mark times where the entire scan of data is plotted in Figure 13. These scans again show the backscatter velocity but plotted at their magnetic backscatter location after accounting for origin field of view. During the interval shown in Figure 12 the interplanetary magnetic field (IMF) geocentric solar magnetospheric (GSM)  $B_y$  component was consistently strong and positive. The GSM  $B_z$  component was weak and negative until 17:00 UT, when it strengthened (remaining negative) until 18:50 UT. After this time GSM  $B_z$  weakened and remained predominantly negative for the rest of the period shown here. Under these IMF conditions, it is expected that an asymmetric twin-cell convection pattern has formed and is expanding equatorward. This convection pattern leads to predominantly westward (sunward) and equatorward flows measured by radars in the dusk flank region, shown in Figure 13.

Looking at Figure 12 (first panel), two patches of backscatter, one at range gates 45–75 and another starting at range gate 45 and shifting closer with time, are seen moving toward the radar between 15:00 and 16:30 UT. At this point the far range gate ionospheric backscatter is no longer seen (slow-moving ionospheric backscatter and groundscatter have appeared instead), though the near-range gate backscatter can still be seen at progressively closer range gates until 18:00 UT, when the Doppler line-of-sight velocity abruptly changes direction. This ionospheric backscatter is detected at progressively increasing range gates. The change in velocity direction coupled with the change in range gate drift suggests that the red patch of ionospheric backscatter seen near range gate 15 at 20:00 UT is the same ionospheric irregularity region shown in blue near range gate 30 at 15:30 UT.

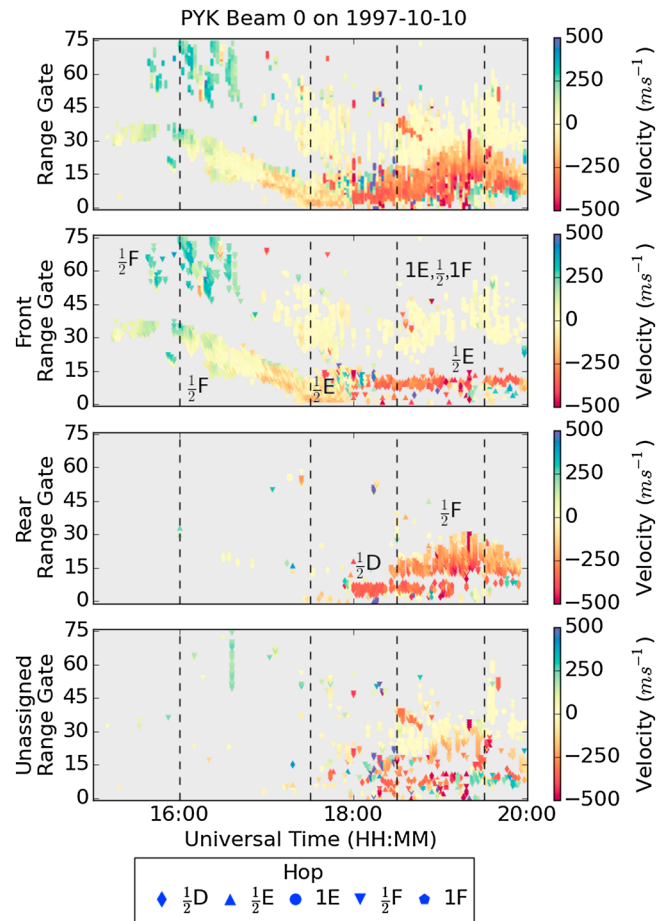


**Figure 12.** Doppler line-of-sight velocity at Pykkvibær for several hours during a geomagnetic storm. (first panel) All backscatter, (second panel) backscatter from the front field of view, (third panel) backscatter from the rear field of view, and (fourth panel) backscatter not assigned to a field of view for each panel in descending order. In Figure 12 (second to third panels) the marker shape denotes the ionospheric propagation path.

The application of the field of view determination method produces origin fields of view and ionospheric propagation paths that support this interpretation. Figure 12 (second panel) shows a patch of  $\frac{1}{2}F$ -hop backscatter (misabeled  $1\frac{1}{2}F$ -hop backscatter due to the large virtual height limit of the  $\frac{1}{2}F$ -hop ceiling, needed to accommodate Pedersen propagation paths) moving toward the radar at far range gates between 15:30 and 16:54 UT. At closer range gates,  $\frac{1}{2}F$ -hop backscatter has been identified and can be seen to be traveling toward the radar across the 16:00 UT front field of view in Figure 13. The variation in line-of-sight velocity across the front field of view, which increases away from beam 0, shows that the irregularity has a large velocity component along beam 0.

The slow-moving, far range gate backscatter is identified primarily (but not exclusively) as  $1F$  groundscatter, while the slow-moving near-range gate backscatter that is seen between 16:00 and 18:00 UT is tagged as  $\frac{1}{2}E$ -hop backscatter. This  $\frac{1}{2}E$  ionospheric backscatter is seen across all beams in the 17:30 UT fields of view in Figure 13. Unlike the 16:00 UT fields of view, there is backscatter close to the radar in the rear field of view at this time. This backscatter was identified as  $\frac{1}{2}D$ -hop backscatter, though this (as well as the other small patches of backscatter assigned to the rear field of view) may be the result of unresolved aliasing. Focusing on the  $F$  region backscatter, the velocities are much smaller at all beams and range gates now at 17:30 UT than they were at 16:00 UT. However, the fastest line-of-sight velocities are still seen at the most eastern beams. Both this and the transport of the  $\frac{1}{2}F$ -hop irregularity from range gates 35–45 to range gates 5–20 demonstrate the movement of plasma toward Iceland.

The ionospheric backscatter that is seen by beam 0 in Figure 12 moving toward the radar until 18:00 UT and then is seen moving away from the radar is labeled  $\frac{1}{2}F$ -hop backscatter and is seen in the front field of view

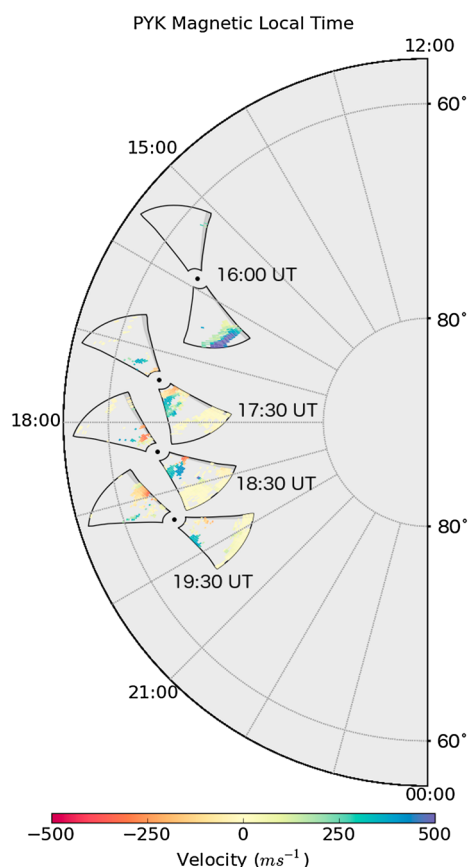


**Figure 13.** Doppler line-of-sight velocity at Pykkvibær for four times selected during a geomagnetic storm on 10 October 1997, placed on a polar map. This map contains magnetic latitudes from 58° to 90°, and magnetic local times (MLT) from noon to midnight. The black circle denotes the radar location, with the front field of view extending northward and the rear field of view extending southward. The distribution of backscatter, accounting for origin field of view, is shown at each UT for the first 45 range gates.

This is not surprising since the phase lag, determined from the cross-correlation function of the combined signals from the main and interferometer arrays will be less reliable when signals from multiple propagation paths are returning to the radar [Farley *et al.*, 1981; Reimer and Hussey, 2015].

Despite a few areas where it was difficult to assign the origin field of view or assign a realistic propagation path, the application of the field of view determination algorithm has made it possible to correctly interpret the direction of the convection pattern over Iceland. If one assumed that all the ionospheric backscatter originates from the front field of view, the velocity directions at 18:30 and 19:30 UT would have been interpreted as northward flows over Iceland, accompanying a shrinking auroral oval. The corrected field of view, in contrast, shows sunward flows associated with an expanding auroral oval, which is consistent with the expected behavior for the prevailing IMF conditions described at the beginning of this section. Applying this field of view determination method to the SuperDARN data used to produce the map potentials will reduce instances of disagreement between different radar observations and improve the spatial coverage.

## 5.2. Groundscatter

The next example looks at the groundscatter seen on 14 December 1995 at Hankasalmi. This date is near the Northern winter solstice, meaning that the *F* region electron density will be low in the front field of view, which covers the polar cap, and sunrise will occur late in the day and be followed closely by sunset. The rear field of view, however, looks out over an area of higher *F* region electron density due to the seasonal anomaly and

when the velocity is positive and in the rear field of view when the velocity is negative. The final fields of view at 18:30 and 19:30 UT in Figure 13 show scans when the  $\frac{1}{2}F$ -hop backscatter seen by beam 0 is in the rear field of view. At these times  $\frac{1}{2}F$ -hop backscatter is also seen in the front field of view at the opposite side of the scan (near beam 15). These velocities indicate that the plasma is flowing sunward and equatorward over Pykkvibær.

Examining the ionospheric backscatter at 19:30 UT in more detail reveals that  $\frac{1}{2}E$ -hop backscatter was assigned to the front field of view around beam 0, while  $\frac{1}{2}D$ - and  $\frac{1}{2}F$ -hop backscatter were assigned to the rear field of view. This separation seems appropriate, since the  $\frac{1}{2}E$ -hop backscatter has a higher velocity than the surrounding  $\frac{1}{2}D$ - and  $\frac{1}{2}F$ -hop backscatter. However, the ionospheric backscatter assigned to the *D* region appears to behave just like the *F* region backscatter. This suggests that while aliasing has not interfered in the field-of-view assignment, it has resulted in an incorrect propagation path assignment. This is to be expected when propagation paths assume triangular propagation paths and do not examine other characteristics that are used to identify ionospheric regions. Treating the  $\frac{1}{2}D$ -hop backscatter as  $\frac{1}{2}F$ -hop backscatter and focusing on the *F* region backscatter, the velocities in both fields of view at 18:30 UT and 19:30 UT present a consistent picture. The largest speeds are seen near the radar at beams 8–15 in front of the radar and beams 0–6 behind the radar, showing the movement of  $\frac{1}{2}F$ -hop irregularities over Pykkvibær, as suggested by Figure 12.

Figure 12 (fourth panel) shows that the algorithm presented here has the most difficulty determining the origin field of view when backscatter was returning from several different propagation paths in the same

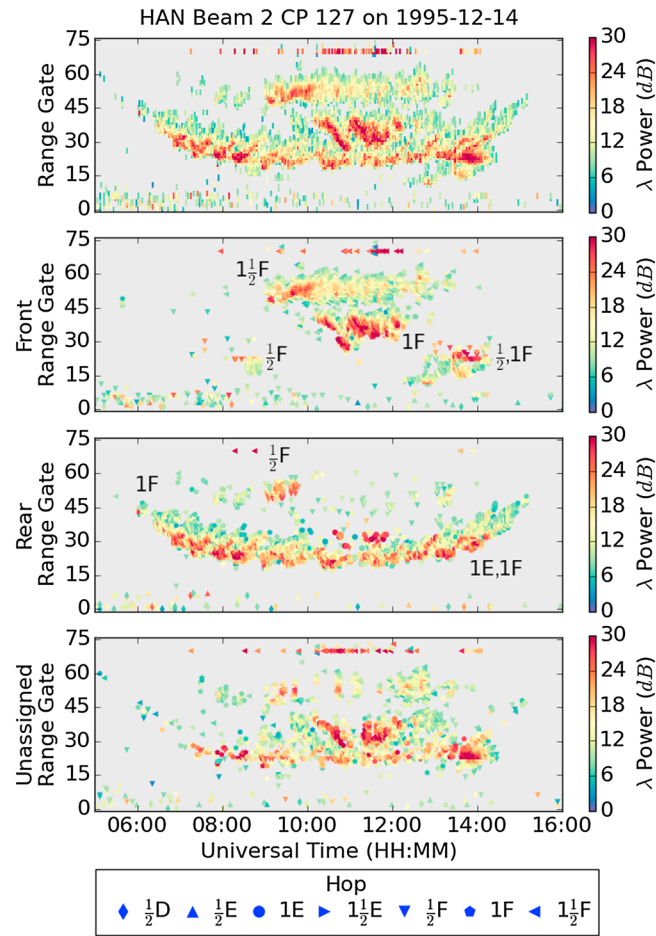


**Figure 14.** Backscatter power at Hankasalmi on 14 December 1995. (first panel) All backscatter, (second panel) backscatter from the front field of view, (third panel) backscatter from the rear field of view, and (fourth panel) backscatter not assigned to a field of view for each panel in descending order. In Figures 14 (second to fourth panels) the marker shape denotes the ionospheric propagation path.

will experience a much longer period of daylight. Thus, it is expected that the front field of view will return groundscatter for a shorter period of time at a further range gate (since a lower electron density allows an HF signal at a given frequency to travel further than a higher electron density would) than the rear field of view.

*Milan et al.* [1997] found this expectation to be true. Figure 9 of *Milan et al.* [1997] presented the backscatter power for Hankasalmi on 14 December 1995 between 05:00 and 16:00 UT. Their figure is reproduced in Figure 14 (first panel). This plot shows an arc of backscatter that begins at range gate 60 on 05:00 UT, moves down to about range gate 20 at 11:00 UT, before moving back up to range gate 45 at 15:00 UT. A much smaller arc can be seen at range gates 45 and 30 between 10:00 and 12:00 UT.

Striations are clearly visible in the backscatter power in both of these arcs. In the larger arc the striations move to larger range gates as time progresses, while in the smaller arc they are angled in the opposite direction. *Milan et al.* [1997] identify these striations as the signature of atmospheric gravity waves propagating toward the equator. The opposing directions of the striations are consistent with a single wave propagating from the pole to the equator if the smaller arc originates in the front field of view and the larger arc originates from the rear field of view.

Figure 14 (second to third panels) confirms the interpretation of *Milan et al.* [1997]. The high-power regions of the smaller arc and the  $1\frac{1}{2}F$ -hop ionospheric backscatter are primarily placed in the front field of view, while the larger arc is primarily placed in the rear field of view. Some notable exceptions are seen. The first is a patch of  $\frac{1}{2}F$ -hop ionospheric backscatter near 08:30 UT, range gate 20 is seen to originate from the front field of view.

This is an appropriate field-of-view assignment; ionospheric backscatter at these latitudes is more likely to occur in darkness (the current situation in the front field of view but not the rear field of view) than in daylight.

The next exception occurs rear fields of view near 11:00 UT, range gate 25–30. These  $1F$  groundscatter observed at these range gates lies at the boundary where  $1F$  groundscatter from the rear field-of-view transitions to  $1F$  groundscatter from the front field of view. Thus, while it is not a problem to see  $1F$  groundscatter at these locations, the power signatures in both the front and rear field of view are more in keeping with the  $1F$  groundscatter from the opposite field of view. This highlights a weakness in the field-of-view identification algorithm in transitional regions.

Another problem region can be seen in the  $\frac{1}{2}F$  ionospheric backscatter near 09:30 and 12:45 UT, range gate 60. This backscatter has been placed in the rear field of view, though the majority of the ionospheric backscatter between 09:30 and 12:45 UT was placed in the front field of view and assigned a  $1\frac{1}{2}F$  propagation path (with some exceptions that were not assigned to either field of view). A reason for this misassignment is that the ionospheric backscatter was observed in fewer beams at the beginning and end of its lifetime. When a backscatter structure spans a small spatial area, it can be difficult to identify the variations in elevation angle.

The final exception lies near 14:00 UT, range gate 20 and consists of a mix of  $\frac{1}{2}F$  and  $1F$  backscatter. This patch can be seen in Figure 14 (first panel) as a high-power region that does not exhibit the striations associated with the rear field-of-view groundscatter. Thus, rather than groundscatter from the rear field of view, it is more appropriately interpreted as ionospheric backscatter from the front field of view with a low line-of-sight velocity along this beam.

Figure 14 (fourth panel) shows that field-of-view assignments were most difficult to make for low-power backscatter (22% of the unassigned points), backscatter with a narrow spatial extent (such as the ionospheric backscatter, most likely noise, at range gate 70), and at places where backscatter from a mix of origin fields of view and propagation path are observed. This is consistent with the results presented in sections 4 and 5.1.

### 5.3. Meteor Ablation

This final example compares a period of two weeks of meteor ablation line-of-sight velocities with coincident neutral wind speeds. When meteoroids enter the atmosphere, they burn up and produce short-lived ion trails in the  $D$  region. The  $D$  region ionosphere drifts with the neutral atmosphere, allowing ionospheric observations in this region to reveal information about the dynamics of the mesosphere and lower thermosphere (MLT). The meteoroid trails are capable of reflecting HF signals and are commonly observed at distances within 400 km of SuperDARN radars [Hall et al., 1997]. Since Doppler line-of-sight velocities will have the wrong sign if they are placed in the wrong field of view, the performance of this detection method for near-range backscatter can be verified by comparing the MLT neutral winds to the meteor ablation drifts.

Meteor ablation is selected using the criteria outlined by Chisham and Freeman [2013] for Saskatoon from beam 0 and beam 15. These two beams were chosen because each beam is aligned with the geographic meridian in one of the fields of view. For beam 0 the line-of-sight velocity is directed north-south in the front field of view, and beam 15 is aligned north-south in the rear field of view, as illustrated in Figure 15 (left). In this figure beam 0 is highlighted in the front field of view in blue, while beam 15 is highlighted in the rear field of view in magenta.

Neutral wind speeds are obtained for the locations that meteor ablation was detected using the 2014 version of the Horizontal Wind Model (HWM14) [Drob et al., 2015]. HWM14 is an empirical model of the neutral winds, which uses over 50 years of ground- and space-based observations from across the globe to provide a statistical view of the quiescent and disturbed neutral winds at a specified altitude between the ground and the exobase. The meridional (north-south) winds are obtained for the time and location of the meteor ablation observations, allowing a comparison to be performed between the SuperDARN observations and the model. Because HWM14 is a statistical model, two weeks of data surrounding the northern winter solstice (14–28 December 2001) are used in the comparison.

Figure 15 (right) show histograms of the differences between the meteor ablation Doppler line-of-sight velocities (with signs adjusted so that the velocities are positive when moving northward in both fields of view) and the HWM14 meridional neutral winds. Figure 15 (right, top) shows the histogram for meteor ablation from the front field of view of beam 0, Figure 15 (right, middle) shows the histogram for the rear field-of-view data from beam 15, and Figure 15 (right, bottom) shows the histogram for beam 0 using the meteor backscatter that was removed from the front field of view (meteor ablation that was placed in the rear field of view or



2001-12-14 to 2001-12-28

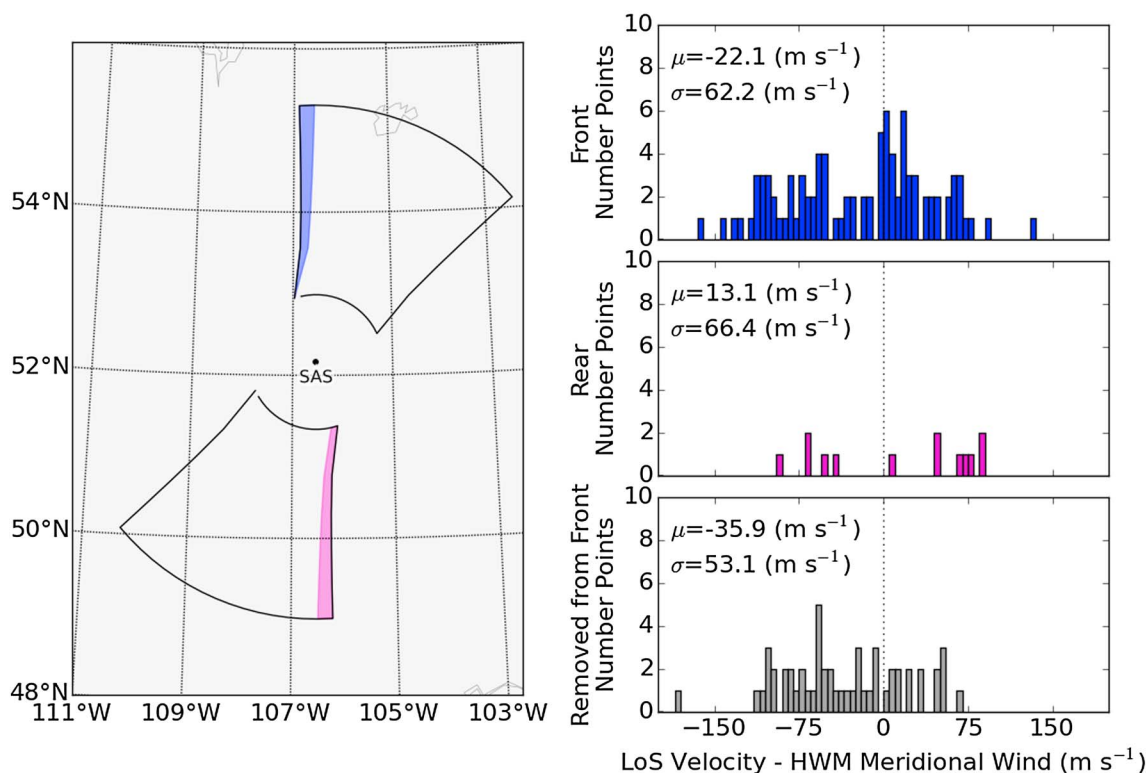


**Figure 15.** Histograms of differences between Doppler line-of-sight (LoS) velocities from meteor ablation at Saskatoon (SAS) and HWM14 meridional neutral winds from the same locations. (left) The geographic region these observations are taken from. To ensure that the Doppler line-of-sight velocities are oriented along the geographic meridian, front field-of-view meteor ablation is selected from beam 0 (highlighted in blue) and rear field-of-view meteor ablation is selected from beam 15 (highlighted in magenta). (right) The histograms of the velocity differences for the front field of view (top), the rear field of view (middle), and the backscatter removed from the front field of view of beam 0 (bottom). The mean ( $\mu$ ) and standard deviation ( $\sigma$ ) of the distributions are also given in each panel.

not assigned a field of view). The histograms used 5 m s<sup>-1</sup> bins for the velocity differences. The means and standard deviations of the differences have also been calculated and are shown in the top left corner of the histogram plots.

Comparing the means and standard deviations shows that the distributions all behave similarly. In each case the mean velocity difference lies close to zero and there are large standard deviations. Examining the histograms, however, shows that the mode of the binned velocity differences for beam 0 is -2.5 m s<sup>-1</sup> when using only meteor ablation assigned to the front field of view (Figure 15 right, top). The mode for unassigned backscatter and backscatter assigned to the rear field of view for beam 0, however, lies near -57.5 m s<sup>-1</sup>. This shows that the agreement between the beam 0 meteor ablation velocities and the HWM14 neutral winds has been improved by selecting backscatter known to originate in the front field of view.

## 6. Conclusions

Ionospheric and ground backscatter has been found to return from both the front and rear fields of view of SuperDARN radars. Incorrectly assuming that all backscatter returns from the front field of view can cause elevation angle errors on the order of tens of degrees and lead to incorrect interpretations of ionospheric convection. However, the origin field of view can be determined using interferometer data. This study presents a method to determine the origin field of view for backscatter detected at SuperDARN radars with an interferometer.

The determination method takes advantage of characteristic patterns seen in the elevation angle to distinguish the origin field of view. This is done in six steps: calculating the virtual height, examining the azimuthal variations in elevation angle, considering the physical limits of the ionosphere, examining the variations in elevation angle along a single beam, testing for consistency in the field of view assigned to spatial structures,



and testing for consistency in the temporal evolution of backscatter. In a test case with ionospheric backscatter returning from a known location (including beams 4–6 at Hankasalmi and beams 13–15 at Þykkvibær), this method correctly identified the field of view for 77.82% of the ionospheric backscatter, misidentified the field of view for 2.09% of the ionospheric backscatter, and was unable to determine a field of view for the remaining 20.09% of the ionospheric backscatter in the regions disturbed by the ionospheric heater at Tromsø. The small percentage of incorrect field-of-view assignments made under the difficult conditions presented by heater-induced ionospheric backscatter demonstrate the robustness of the field-of-view detection algorithm.

Several different types of SuperDARN backscatter were processed using the field-of-view determination method, including groundscatter, *E* and *F* region ionospheric backscatter, and meteor ablation. In all cases that reexamined previously published data, the origin fields of view were found to be consistent with the previously posited physical explanations. The (previously unpublished) case of an *F* region irregularity apparently changing direction as the polar cap expanded is now clearly seen to travel past the radar, moving from the front to the rear field of view. Groundscatter observations separated into front and rear fields of view clearly showed the difference in sunrise on either side of the radar and also showed a consistent pattern of atmospheric gravity waves. Finally, meteor ablation assigned to the front field of view was seen to show better agreement with climatological neutral wind speeds when backscatter assigned to the rear field of view or no field of view was removed. Thus, this study has established the importance of accounting for the origin field of view when using ionospheric and ground backscatter from a HF coherent scatter radar (such as those that make up SuperDARN) and presented a reliable automated method to accurately determine the origin field of view. The application of this method to HF radar data processing will reduce the error in location-dependent quantities, such as elevation angle, virtual height, and the Doppler velocity.

#### Acknowledgments

This study was supported by NERC grant NE/K011766/1. We gratefully acknowledge the funding support from the Canadian Space Agency (CSA) for the e-POP project and from the Natural Science and Engineering Research Council of Canada (NSERC) under the Discovery Grants and Discovery Accelerator Supplements Programs. A python implementation of this detection process is available as part of the DaViTpy python toolkit in the `davitpy/pydarn/proc/fov` directory. The Virginia Tech SuperDARN database ([sftp://sd-data.ece.vt.edu](http://sd-data.ece.vt.edu)) is automatically accessed by the DaViTpy python toolkit. This toolkit contains up-to-date public access usernames and passwords that may be used to access the data without installing DaViTpy.

#### References

- André, D., G. J. Sofko, K. Baker, and J. MacDougall (1998), SuperDARN interferometry: Meteor echoes and electron densities from groundscatter, *J. Geophys. Res.*, **103**, 7003–7015, doi:10.1029/97JA02923.
- Bland, E. C., A. J. McDonald, and S. Larquier (2014), Determination of ionospheric parameters in real time using SuperDARN HF Radars, *J. Geophys. Res. Space Physics*, **119**, 5830–5846, doi:10.1002/2014JA020076.
- Chisham, G., and M. P. Freeman (2013), A reassessment of SuperDARN meteor echoes from the upper mesosphere and lower thermosphere, *J. Atmos. Sol. Terr. Phys.*, **102**, 207–221, doi:10.1016/j.jastp.2013.05.018.
- Chisham, G., et al. (2007), A decade of the Super Dual Auroral Radar Network (SuperDARN): Scientific achievements, new techniques and future directions, *Surv. Geophys.*, **28**(1), 33–109, doi:10.1007/s10712-007-9017-8.
- Chisham, G., T. K. Yeoman, and G. J. Sofko (2008), Mapping ionospheric backscatter measured by the SuperDARN HF radars. Part 1: A new empirical virtual height model, *Ann. Geophys.*, **26**(4), 823–841, doi:10.5194/angeo-26-823-2008.
- Drob, D. P., et al. (2015), An update to the Horizontal Wind Model (HWM): The Quiet Time Thermosphere, *Earth Space Sci.*, **2**, 301–319, doi:10.1002/2014EA000089.
- Farley, D. T., H. M. Ierick, and B. G. Fejer (1981), Radar interferometry: A new technique for studying plasma turbulence in the ionosphere, *J. Geophys. Res.*, **86**(A3), 1467–1472, doi:10.1029/JA086iA03p01467.
- Greenwald, R. A., et al. (1995), DARN/SUPERDARN, *Space Sci. Rev.*, **71**(1–4), 761–796, doi:10.1007/BF00751350.
- Hall, G. E., J. W. MacDougall, D. R. Moorcroft, J. P. St Maurice, A. H. Manson, and C. E. Meek (1997), Super Dual Auroral Radar Network observations of meteor echoes, *J. Geophys. Res.*, **102**(A7), 14,603–14,614, doi:10.1029/97JA00517.
- James, H. G., E. P. King, A. White, R. H. Hum, W. H. H. L. Lunscher, and C. L. Siefring (2015), The e-POP radio receiver instrument on CASSIOPE, *Space Sci. Rev.*, **189**(1), 79–105, doi:10.1007/s11214-014-0130-y.
- McDonald, A. J., J. Whittington, S. de Larquier, E. Custovic, T. A. Kane, and J. C. Devlin (2013), Elevation angle-of-arrival determination for a standard and a modified SuperDARN HF radar layout, *Radio Sci.*, **48**, 709–721, doi:10.1002/2013RS005157.
- Milan, S. E., T. B. Jones, T. R. Robinson, E. C. Thomas, and T. K. Yeoman (1997), Interferometric evidence for the observation of ground backscatter originating behind the CUTLASS coherent HF radars, *Ann. Geophys.*, **15**(1), 29–39, doi:10.1007/s00585-997-0029-y.
- Reimer, A. S., and G. C. Hussey (2015), Estimating self-clutter of the multiple-pulse technique, *Radio Sci.*, **50**, 698–711, doi:10.1002/2015RS005706.
- Sterne, K. T., R. Greenwald, J. B. H. Baker, and J. M. Ruohoniemi (2011), Modeling of a twin terminated folded dipole antenna for the Super Dual Auroral Radar Network (SuperDARN), in *Radar Conference (RADAR)*, pp. 934–938, IEEE, Kansas City, Mo., doi:10.1109/RADAR.2011.5960673.
- Yau, A. W., and H. G. James (2015), CASSIOPE enhanced Polar Outflow Probe (e-POP) mission overview, *Space Sci. Rev.*, **189**(1), 3–14, doi:10.1007/s11214-015-0135-1.
- Yeoman, T. K., D. M. Wright, A. J. Stocker, and T. B. Jones (2001), An evaluation of range accuracy in the Super Dual Auroral Radar Network over-the-horizon HF radar systems, *Radio Sci.*, **36**(4), 801–813, doi:10.1029/2000RS002558.